

# STAvatar: Soft Binding and Temporal Density Control for Monocular 3D Head Avatars Reconstruction

Jiankuo Zhao<sup>1,2</sup>, Xiangyu Zhu<sup>1,2\*</sup>, Zidu Wang<sup>1,2</sup>, Zhen Lei<sup>1,2,3</sup>

<sup>1</sup>MAIS, Institute of Automation, Chinese Academy of Sciences

<sup>2</sup>School of Artificial Intelligence, University of Chinese Academy of Sciences

<sup>3</sup>Centre for Artificial Intelligence and Robotics, Hong Kong Institute of Science & Innovation, Chinese Academy of Sciences

{zhaojiankuo2024, xiangyu.zhu, zhen.lei}@ia.ac.cn

{wangzidu0705}@gmail.com

## Abstract

Reconstructing high-fidelity and animatable 3D head avatars from monocular videos remains a challenging yet essential task. Existing methods based on 3D Gaussian Splatting typically bind Gaussians to mesh triangles and model deformations solely via Linear Blend Skinning, which results in rigid motion and limited expressiveness. Moreover, they lack specialized strategies to handle frequently occluded regions (e.g., mouth interiors, eyelids). To address these limitations, we propose STAvatar, which consists of two key components: (1) a UV-Adaptive Soft Binding framework that leverages both image-based and geometric priors to learn per-Gaussian feature offsets within the UV space. This UV representation supports dynamic re-sampling, ensuring full compatibility with Adaptive Density Control (ADC) and enhanced adaptability to shape and textural variations. (2) a Temporal ADC strategy, which first clusters structurally similar frames to facilitate more targeted computation of the densification criterion. It further introduces a novel fused perceptual error as clone criterion to jointly capture geometric and textural discrepancies, encouraging densification in regions requiring finer details. Extensive experiments on four benchmark datasets demonstrate that STAvatar achieves state-of-the-art reconstruction performance, especially in capturing fine-grained details and reconstructing frequently occluded regions. The code will be publicly available.

## 1. Introduction

Reconstructing animatable and photo-realistic 3D head avatars has been a longstanding problem in computer vi-

\*Corresponding author

Project page: <https://lcfaw.github.io/STAvatar/>.

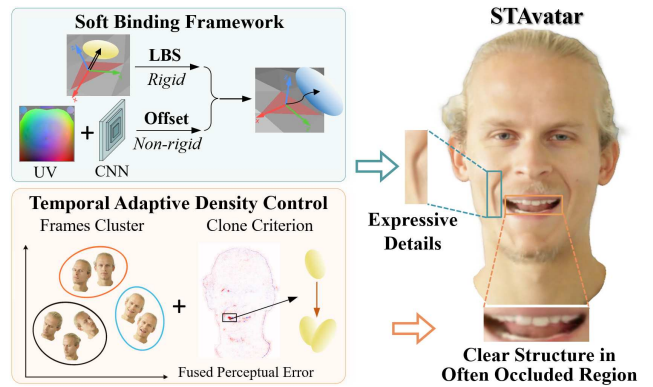


Figure 1. STAvatar proposes a Soft Binding framework and a Temporal Adaptive Density Control strategy to reconstruct high-fidelity 3D head avatars from monocular videos.

sion and graphics [3, 22, 27], driven by growing demands in AR/VR, telepresence, digital humans and interactive media. To achieve high-quality avatar reconstruction, conventional methods typically rely on expensive multi-camera systems [7, 30] which require complex manual setups and are impractical for consumer-level deployment. In contrast, monocular-based approaches [6, 25, 35] aim to produce high-fidelity results using a single consumer-grade camera, enabling broader accessibility in immersive and personalized virtual environments.

Recent years have witnessed the emergence of 3D Gaussian Splatting (3DGS) [8] as a powerful volumetric representation, delivering both high-fidelity rendering and real-time performance in neural scene reconstruction. Building on its success in static scenes, many works have explored its application to animatable 3D head avatar reconstruction. These methods typically follow a two-stage pipeline: a parametric head-tracking algorithm [19, 39] is first employed to estimate the facial pose, expression, and shape for

each frame; subsequently, Gaussian primitives are bound to mesh triangles and driven by a deformation field, which is typically implemented using Linear Blend Skinning (LBS) [20]. During training, each Gaussian’s parameters are optimized via differentiable rendering to minimize photometric loss. Despite achieving enhanced visual fidelity and animation realism, existing Gaussian-based approaches still face several open challenges. To address these limitations, we propose STAvatar, as shown in Fig. 1, and provide a detailed explanation below.

First, existing animatable reconstruction methods often suffer from rigid connection between Gaussian primitives and mesh triangles, resulting in poor handling of non-rigid and fine-scale deformations. Fig. 2(a) illustrates this simple hard binding framework [24, 31] in which each Gaussian deforms solely according to the LBS of its parent triangle. Although this enables basic animation control, it fails to model fine-grained deformations, as the Gaussians remain relatively static within the triangle’s local coordinate frame. This limitation stems from the gap between mesh and Gaussian representations. While meshes inherently encode topology and support native skinning for deformation, Gaussians are structureless and rely on externally defined deformation fields to capture complex motions and fine details such as facial wrinkles. Some methods [1, 5, 28] attempt to enhance each Gaussian’s deformation using a fixed-dimension multilayer perceptron (MLP). However, this design requires predefining a fixed number of Gaussians, which is suboptimal since different identities often demand varying Gaussian densities. Besides, it neglects spatial context and may be incompatible with the Adaptive Density Control (ADC) inherent to 3DGS. To enhance deformation ability while preserving the flexibility of ADC, STAvatar proposes a UV-Adaptive Soft Binding framework, which integrates the LBS for coarse deformation and a dual-branch network for fine-detail recovery. By generating a feature offset map in UV space, STAvatar leverages spatial context to model the Gaussian deformation field and enables arbitrary-resolution sampling to support ADC.

Second, the vanilla ADC in 3DGS is tailored for static scene reconstruction and fails to handle transiently visible or frequently occluded regions in dynamic avatar reconstruction. As illustrated in Fig. 2(b), certain regions (*e.g.*, mouth interiors) are only visible in a subset of frames and contribute minimally to rendering when occluded. This results in low average criterion—such as the positional gradient used in 3DGS—which impedes sufficient densification. In addition, as shown in Fig. 2(c), the positional gradient in 3DGS only captures geometric discrepancies while neglecting texture details [21], which leads to the omission of regions with high texture errors and the failure to add Gaussians to these regions. To address these limitations of ADC, STAvatar propose a Temporal Adaptive Density

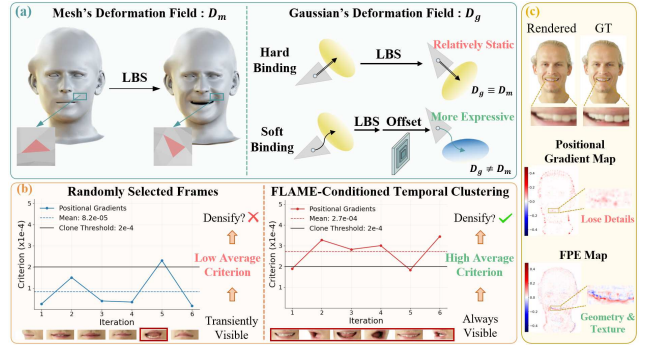


Figure 2. Limitations of existing research. (a) Hard binding forces Gaussians to remain relatively static within the triangle coordinate frames, thereby limiting their ability to capture fine-grained details. (b) Transiently visible regions, such as mouth interiors, often exhibit low average positional gradients, which impedes effective Gaussian densification. (c) The positional gradient only reflects geometric inconsistencies and often loses texture details, which hinders the addition of Gaussians in high-frequency regions.

Control strategy incorporating FLAME-Conditioned Temporal Clustering (FTC) and a Fused Perceptual Error with Average-Peak Criterion (FPE-AP). As shown in Fig. 2(b), FTC partitions frames into structure-coherent clusters to encourage frequently occluded regions remain visible within a cluster, facilitating targeted refinement. FPE-AP replaces positional gradients by directly estimating each Gaussian’s fused perceptual error, which jointly considers both geometric and textural discrepancies. Besides, FPE-AP selects Gaussians exhibiting the highest instantaneous errors across iterations to better capture regions with large peak errors.

Finally, we evaluate STAvatar through extensive experiments on four datasets, demonstrating clear improvements over existing methods in recovering fine details and handling challenging regions such as mouth interiors and eyelids. Besides, STAvatar exhibits accurate cross-reenactment performance, highlighting its potential in real-world applications. Our main contributions are as follows:

- We propose a UV-Adaptive Soft Binding framework that supports both soft binding and ADC of 3DGS in animatable Gaussian avatar reconstruction.
- We propose a Temporal ADC strategy incorporating FTC and FPE-AP which enhances the ADC in dynamic Gaussian avatar reconstruction.
- We conduct experiments on various datasets, demonstrating superior rendering quality, improved detail reconstruction, and more accurate cross-reenactment.

## 2. Related Work

### 2.1. Gaussian Head Reconstruction

3DGS [8] has recently emerged as a flexible and efficient approach for 3D scene representation. By employing a large

number of anisotropic Gaussian primitives—each parameterized by geometry and appearance attributes—it achieves high-quality reconstructions, making it particularly well-suited for detailed human head modeling. To enable avatar driving, typical methods [16, 20, 23–25, 31] adopt a hard-binding framework that associates Gaussians with mesh triangles to transfer mesh motion via LBS, which, however, fails to bridge the inherent gap between mesh and Gaussian representations, leading to suboptimal performance in handling complex motions and expressions. Alternatively, other approaches [1, 14, 28, 29] leverage MLP to predict per-Gaussian attribute offsets, thereby achieving a more flexible soft-binding framework. However, these methods often neglect ADC by using a fixed number of Gaussians across different identities, which limits expressiveness and reconstruction quality. In addition, several studies [12, 17, 41] propose to represent avatars with a base model and a set of expression blendshapes. Although these methods can achieve high training efficiency, they often suffer from low fidelity or produce blurred results under large pose variations, since the learned blendshapes may not adequately capture diverse pose-dependent deformations.

## 2.2. Adaptive Density Control of 3DGS

ADC strategy is a key module in 3DGS which dynamically clones, splits and prunes Gaussians to balance detail preservation and representation compactness. The vanilla ADC selects primitives for densification based on average positional gradients and Gaussian scales. However, this heuristic often results in underfitting and blurred details, as it neglects texture-related cues and only focus average criterion. To overcome these limitations, some recent works [10, 18, 21, 34, 37] revise the densification criterion to incorporate richer information, thereby achieving finer details in underrepresented regions. Besides, optimization-theoretic approaches have been proposed to establish more principled rules for cloning and splitting: SteepGS [26] leverages steepest-descent analysis to trigger Gaussian splits, whereas 3DGS-MCMC [9] formulates density control as a Markov Chain Monte Carlo (MCMC) sampling process with  $L_1$ -regularized pruning. More recently, Efficient Density Control [2] introduces long-axis splitting operations and recovery-aware pruning strategies to reduce redundant Gaussians and accelerate convergence, while Gradient-Direction-Aware ADC [38] incorporates gradient coherence and angular alignment to more effectively determine which Gaussians should be cloned or split. However, as these methods are primarily tailored for static scene reconstruction, they tend to under-fit transiently visible regions and fail to jointly consider both geometric and textural discrepancies.

## 3. Method

We first introduce the general Gaussian avatar reconstruction pipeline in Sec. 3.1. Next, we present a UV-Adaptive Soft Binding framework in Sec. 3.2. The Temporal Adaptive Density Control strategy, which integrates FLAME-Conditioned Temporal Clustering (FTC) and a Fused Perceptual Error with Average-Peak Criterion (FPE-AP), is discussed in Sec. 3.3. Finally, the detailed optimization process is described in Sec. 3.4.

### 3.1. Preliminaries

**Initialization.** Following [20], we initialize Gaussian primitives  $g_i$  based on the tracked FLAME model. Each  $g_i$  is bound to a mesh triangle and parameterized by a center position  $\mu$ , a scale matrix  $S$ , and a rotation matrix  $R$  defined on the canonical FLAME mesh [13]. The 3D Gaussian density is defined as:

$$G(\mathbf{x}) = e^{-\frac{1}{2}(\mathbf{x}-\mu)^T \Sigma^{-1}(\mathbf{x}-\mu)}, \quad (1)$$

where  $\Sigma = \mathbf{R} \mathbf{S} \mathbf{S}^T \mathbf{R}^T$  to keep the covariance matrix positive. In addition to geometric parameters, each primitive also carries appearance attributes: opacity  $\alpha$  and color  $c$ .

**Animate.** To animate these canonical primitives according to FLAME deformations, we first transform their parameters using the parent triangle’s barycentric mapping to get the coarsely estimated parameters  $\theta = \{\tilde{\mu}, \tilde{s}, \tilde{r}, \tilde{\alpha}, \tilde{c}\}$ . Specifically,

$$\tilde{r} = \mathbf{r} \mathbf{R}, \quad \tilde{\mu} = k \mathbf{r} \mu + \mathbf{t}, \quad \tilde{s} = k \mathbf{s}, \quad \tilde{\alpha} = \alpha, \quad \tilde{c} = c, \quad (2)$$

where  $\mathbf{r}$  and  $\mathbf{t}$  denote the triangle’s relative rotation and barycenter translation, respectively, and the isotropic scale  $k$  reflects the triangle’s size.

**Render.** Given the final parameters  $\theta^*$  (see Sec. 3.2), the rendered color  $C$  of a pixel is obtained by compositing all overlapping primitives in a depth-sorted compositing:

$$C = \sum_{i=1}^N c_i^* \alpha_i' \prod_{j=1}^{i-1} (1 - \alpha_j'), \quad (3)$$

where  $c_i^*$  is the RGB color encoded via 3rd-degree spherical harmonics, and  $\alpha_i'$  is the 2D projected opacity obtained by evaluating the Gaussian’s contribution in image space. This compositing accounts for occlusion by sorting the primitives according to their depth values.

### 3.2. UV-Adaptive Soft Binding Framework

Eq. (2) only yields a coarse deformation for each Gaussian  $g_i$ , failing to capture fine details or appearance changes since opacity  $\tilde{\alpha}$  and color  $\tilde{c}$  remain constant under LBS. To address this while preserving the flexibility of ADC, we introduce the UV-Adaptive Soft Binding framework.

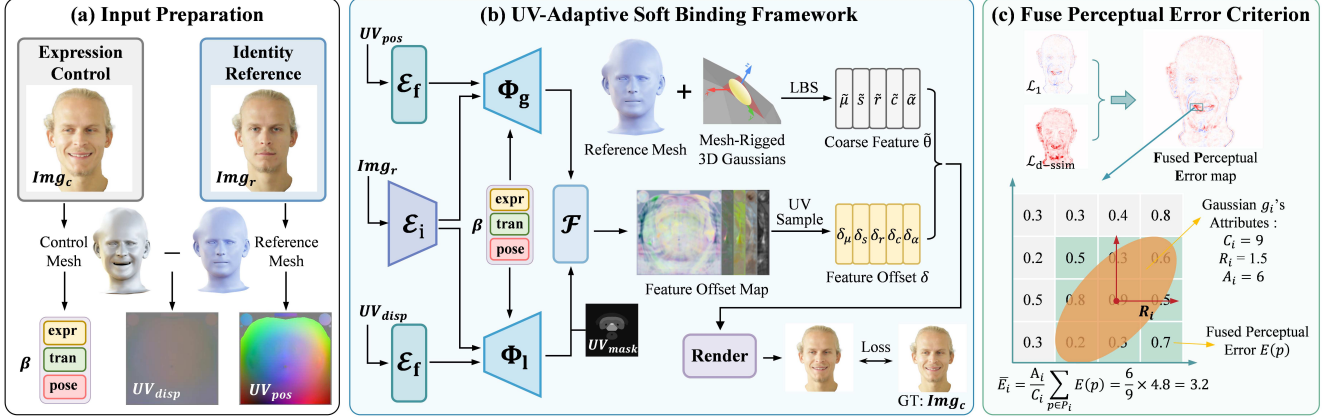


Figure 3. Overview of STAvatar. (a) In addition to a fixed identity reference image and its UV position map, we further rasterize the vertex offsets between reference mesh and control mesh to obtain a UV displacement map as input. (b) We construct a dual-branch network to predict a feature offset map in UV space, from which an offset  $\delta_i$  is sampled for each Gaussian  $g_i$ . This offset is added to the coarsely estimated parameters  $\tilde{\theta}$  to get final parameters  $\theta^*$ . The final images are then rendered using Gaussian Splatting. (c) We first construct a perceptual error map by combining  $\mathcal{L}_1$  map and  $\mathcal{L}_{d-ssim}$  map. Then, we estimate the 2D projection of each Gaussian  $g_i$  using the recorded attributes, based on which the fused perceptual error is computed.

**Input Preparation.** As shown in Fig. 3(a), after tracking the flame model for video frames, we select a fixed reference image  $Img_r$  to extract the texture input and rasterize its UV position map  $UV_{pos}$  to obtain UV coordinate information. To further enhance the capacity for deformation modeling, we rasterize the vertex offsets between the reference mesh and the control mesh into UV space to generate an additional input  $UV_{disp}$ .

**Soft Binding.** Fig. 3(b) illustrates our dual-branch network, which estimates per-Gaussian feature offsets in UV space to capture rich spatial context. We first extract texture features  $T$  by encoding  $Img_r$  with a U-Net encoder, denoted as  $\mathcal{E}_i$ , such that  $T = \mathcal{E}_i(Img_r)$ . These features are then concatenated with Fourier positional encoded position maps  $UV'_{pos} = \mathcal{E}_f(UV_{pos})$  and displacement maps  $UV'_{disp} = \mathcal{E}_f(UV_{disp})$ . Besides, both branches  $\Phi_g$  and  $\Phi_l$  take as input a control code  $\beta$ , formed by concatenating expression, translation, and pose codes, to model Gaussian deformations. The decoded outputs,  $\omega_g$  and  $\omega_l$ , are then fused to generate the final feature offset map  $\Delta_{map} \in \mathbb{R}^{256 \times 256 \times 13}$ , where each texel stores a 13-dimensional Gaussian offset. The entire process can be described as:

$$\omega_g = \Phi_g(T, UV'_{pos}, \beta), \quad (4)$$

$$\omega_l = \sum_{i=1}^4 H_i(M_i \odot \Phi_l(T, UV'_{disp}, \beta)), \quad (5)$$

$$\Delta_{map} = \mathcal{F}(\omega_g, \omega_l), \quad (6)$$

where  $M_i \in \{0, 1\}^{256 \times 256}$  denotes the UV spatial mask for the  $i$ -th facial region, including the eyes, mouth, nose, and forehead, and  $\odot$  denotes the element-wise (Hadamard) product. The local branch  $\phi_l$  shares a common decoder

across all regions and applies region-specific decoding heads  $H_i$  to the masked features. Note that  $Img_r$  can be selected randomly; in our experiments, we default to using the first frame.

**UV-Adaptive Sampling.** We sample each Gaussian  $g_i$ 's offset  $\delta_i = \{\delta_\mu, \delta_s, \delta_r, \delta_\alpha, \delta_c\}$  from the feature offset map  $\Delta_{map}$  by assigning each  $g_i$  a UV coordinate via our UV-Adaptive Sampling, which is updated upon densification to accommodate dynamic changes in Gaussian count. A brief algorithmic description of this sampling procedure is provided in Algorithm 1, with a detailed version included in the supplementary material. After sampling, we apply different activation functions to ensure numerical stability and constrain the effect of the predicted offsets  $\delta_i$  (details in Appendix). The final Gaussian parameters  $\theta^*$  are then computed as:

$$\begin{aligned} \mu^* &= \tilde{\mu} + \delta_\mu, & c^* &= \tilde{c} + \delta_c, & \alpha^* &= \tilde{\alpha} + \delta_\alpha, \\ s^* &= \tilde{s} \odot \delta_s, & r^* &= q(\tilde{r}, \delta_r), \end{aligned} \quad (7)$$

where  $q(\cdot, \cdot)$  represents the Hamilton product between two unit quaternions, used to compose the rotation  $\tilde{r}$  and its predicted offset  $\delta_r$ . After obtaining the final parameters  $\theta^*$ , we employ Eq. (3) to render the images.

### 3.3. Temporal Adaptive Density Control

**FPE-AP.** To identify Gaussians that require cloning, we introduce a more interpretable and comprehensive criterion, FPE-AP, which directly indicates regions exhibiting significant geometric or texture errors that may benefit from more Gaussian primitives. Since the error at each pixel is influenced by multiple overlapping Gaussians, it is computation-

---

**Algorithm 1** UV-Adaptive Sampling
 

---

**Input:** Face bindings  $\mathcal{B}$ , UV vertices  $\mathcal{V}_{uv}$ , UV faces  $\mathcal{F}_{uv}$ 
**Output:**  $\mathcal{U} \in \mathbb{R}^{N \times 2}$ : UV coordinates per Gaussian
 

---

- 1:  $(\mathcal{M}_{face}, \mathcal{M}_{zbary}) \leftarrow \text{Rasterize}(\mathcal{V}_{uv}, \mathcal{F}_{uv})$
  - 2: Build per-face pixel pool  $\mathcal{P}$  from  $\mathcal{M}_{face}$
  - 3:  $\mathcal{F}_{valid} \leftarrow \{f \in \mathcal{F}_{uv} \mid \mathcal{P}[f] \neq \emptyset\}$
  - 4: Initialize empty barycentric buffer  $\mathbf{b}$  and face index buffer  $\mathbf{f}_{idx}$
  - 5: **for** each face  $f$  in face bindings  $\mathcal{B}$  **do**
  - 6:    $C_f \leftarrow$  count of points bound to face  $f$
  - 7:    $\mathcal{I}_f \leftarrow$  indices of points bound to face  $f$
  - 8:   **if**  $f \in \mathcal{F}_{valid}$  **then**
  - 9:      $\mathbf{p}_f \leftarrow$  pixel list for face  $f$  from  $\mathcal{P}$
  - 10:     Sample  $C_f$  pixels from  $\mathbf{p}_f$
  - 11:     Extract corresponding barycentric coordinates  $\mathbf{b}_f$
  - 12:   **else**
  - 13:     Analytically sample  $C_f$  barycentric coordinates  $\mathbf{b}_f$
  - 14:   **end if**
  - 15:   Assign  $\mathbf{b}_f$  to  $\mathbf{b}[\mathcal{I}_f]$ , and fill  $\mathbf{f}_{idx}[\mathcal{I}_f] \leftarrow f$
  - 16: **end for**
  - 17:  $\mathcal{U} \leftarrow \text{BarycentricReweight}(\mathcal{V}_{uv}, \mathcal{F}_{uv}, \mathbf{f}_{idx}, \mathbf{b})$
- 

ally intractable and inefficient to compute the exact contribution of each individual Gaussian.

To address this, as illustrated in Fig. 3(c), we first construct a fused perceptual error map:

$$E = (1 - \lambda_1) |\mathcal{L}_1| + \lambda_1 \mathcal{L}_{d\text{-ssim}}, \quad (8)$$

where  $\mathcal{L}_1$  denotes the per-pixel absolute difference, and  $\mathcal{L}_{d\text{-ssim}}$  represents the per-pixel dissimilarity, derived from the Structural Similarity Index (SSIM). We set  $\lambda_1 = 0.2$  to keep it consistent with the RGB loss design in Eq. (12), which better aligns with human perceptual sensitivity.

To estimate each Gaussian’s 2D projection for fused perceptual error calculation, we record its screen-space center  $(x_i, y_i)$ , total number of covered pixels  $C_i$ , and accumulated alpha blending weight  $A_i = \sum_{p \in \mathcal{P}_i} a_i(p)$ , where  $a_i(p)$  is the blending weight of  $g_i$  at pixel  $p$ . The influence region is defined as a square centered at  $(x_i, y_i)$  with half-extent  $R_i = \lfloor \frac{\sqrt{C_i}}{2} \rfloor$ , and the corresponding pixel set  $\mathcal{P}_i$  includes all pixels within this region. We then approximate the average fused perceptual error for  $g_i$  as

$$\bar{E}_i = \frac{A_i}{C_i} \sum_{p \in \mathcal{P}_i} E(p), \quad (9)$$

where all window-sum computations are efficiently accelerated using a two-dimensional summed-area table (details in the supplementary material).

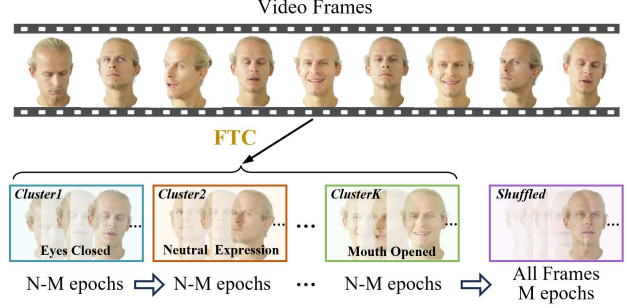


Figure 4. FLAME-Conditioned Temporal Clustering. We cluster video frames into  $K$  clusters and conduct ADC within each cluster’s training.

Furthermore, to capture transient spikes, we define a peak fused perceptual error across all iterations  $t$  as

$$E_i^{\text{peak}} = \max_t \left( \frac{A_i^{(t)}}{C_i^{(t)}} \sum_{p \in \mathcal{P}_i^{(t)}} E^{(t)}(p) \right), \quad (10)$$

and select top 3% Gaussians by  $E_i^{\text{peak}}$  to form the set  $\mathcal{S}_{\text{peak}}$ . Finally, Gaussian  $g_i$  is cloned if

$$\bar{E}_i > \tau_{\text{avg}} \quad \text{or} \quad i \in \mathcal{S}_{\text{peak}}, \quad (11)$$

where  $\tau_{\text{avg}} = 1 \times 10^{-3}$ . Note that, for Gaussian splitting, we still use the positional gradient as criterion since splitting is primarily driven by geometric inconsistency.

**FTC.** As shown in Fig. 4, we cluster video frames into  $K$  clusters based on their FLAME parameters (expression, pose, and translation), with respective weights of 0.3, 0.6, and 0.1. Before clustering, we apply Principal Component Analysis (PCA) to reduce the parameter dimensionality for more effective distance computation. We then perform K-means clustering, which ensures the densification criterion is computed among structurally similar frames. This strategy mitigates insufficient densification in transiently visible regions. To accommodate different identities, we select  $K$  within [5, 12] by maximizing the average silhouette score.

During training, each cluster is first optimized for  $N - M$  epochs, during which ADC is applied. After all clusters have been trained, we conduct additional  $M$  epochs using randomly shuffled data to mitigate potential inconsistencies introduced by inter-cluster variations. In our experiments, we set  $N = 6$  and  $M = 1$ .

### 3.4. Training Objective and Optimization

**RGB Loss.** We supervise the rendered images using a combination of  $\mathcal{L}_1$  term and D-SSIM term following [8]. To better capture high-frequency facial details, we further introduce the perceptual loss  $\mathcal{L}_{\text{vgg}}$ , which is activated only in the second half of training to balance performance and

Table 1. Comparison of quantitative results with state-of-the-art methods. The **best** and **second** are highlighted, respectively.

Method	INSTA Dataset			PointAvatar Dataset			NerFace Dataset			HDTF Dataset		
	PSNR↑	SSIM↑	LPIPS↓	PSNR↑	SSIM↑	LPIPS↓	PSNR↑	SSIM↑	LPIPS↓	PSNR↑	SSIM↑	LPIPS↓
SA [24]	27.48	0.9329	0.1046	24.93	0.8938	0.1478	26.14	0.9238	0.1145	26.02	0.8922	0.1821
MGA [1]	27.34	0.9351	0.0859	27.91	0.9277	0.1113	26.52	0.9333	0.0900	27.04	0.9171	0.1225
GA [20]	26.98	0.9378	0.0851	24.62	0.9073	0.1333	25.74	0.9279	0.0965	25.08	0.8879	0.1763
FA [28]	27.90	0.9357	0.0563	26.19	0.9055	0.0947	26.96	0.9331	0.0555	26.83	0.9110	0.0774
RGBA [12]	28.41	0.9493	0.0518	26.67	0.9217	0.0883	27.13	0.9438	0.0550	26.72	0.9277	0.0821
Fate [31]	28.33	0.9446	0.0508	28.36	0.9287	0.0776	27.12	0.9364	0.0558	27.18	0.9187	0.0849
Ours	30.63	0.9587	0.0304	28.25	0.9337	0.0495	30.08	0.9567	0.0311	27.99	0.9315	0.0542

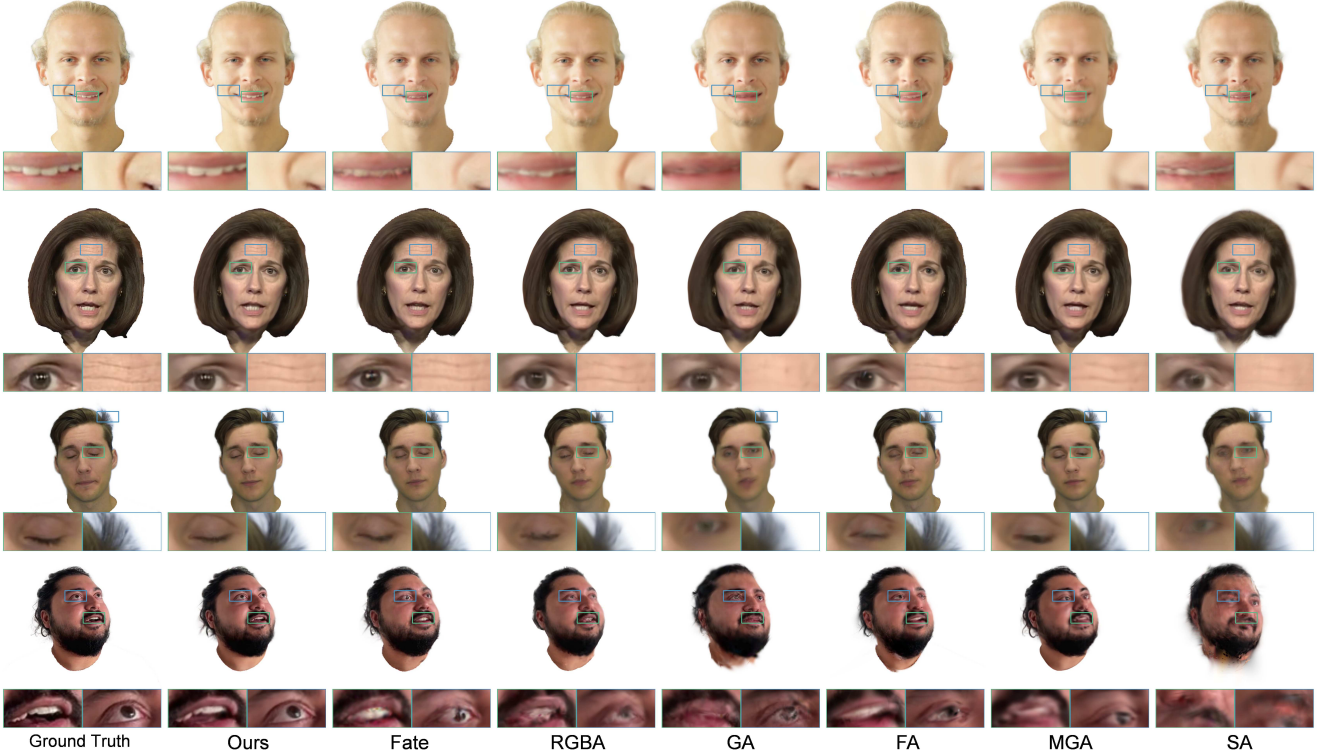


Figure 5. Qualitative results of head avatar reconstruction. Our method recovers finer details and delicate structures such as wrinkles and teeth. Moreover, it produces clearer results in challenging regions like mouth interiors and eyelids.

efficiency. The overall image loss is defined as:

$$\mathcal{L}_{\text{rgb}} = (1 - \lambda_1)\mathcal{L}_1 + \lambda_1\mathcal{L}_{\text{d-ssim}} + \gamma\lambda_2\mathcal{L}_{\text{vgg}}, \quad (12)$$

where  $\lambda_1 = 0.2$ ,  $\lambda_2 = 0.05$ , and  $\gamma = 1$  only during the latter half of training.

**Regularization Loss.** To regularize the predicted offset  $\delta_i$ , we apply a regularization term to constrain the scale and color offsets:

$$\mathcal{L}_{\text{offset}} = \lambda_3|\delta_s - 1| + \lambda_4\delta_c, \quad (13)$$

where  $\lambda_3 = 0.01$  and  $\lambda_4 = 0.001$ . Following GaussianAvatars [20], we also employ a position loss and a scale loss

to regularize the spatial alignment and local scale of the 3D Gaussians with respect to their parent triangles.

The total training loss is thus defined as:

$$\mathcal{L} = \mathcal{L}_{\text{rgb}} + \mathcal{L}_{\text{offset}} + \lambda_p\mathcal{L}_{\text{position}} + \lambda_s\mathcal{L}_{\text{scale}}, \quad (14)$$

where  $\lambda_p = 0.01$  and  $\lambda_s = 1$ .

**Optimization.** We employ Adam [11] for parameter optimization, using identical hyperparameter settings across all subjects. The learning rate is set to  $1 \times 10^{-4}$  for the UV-Adaptive Soft Binding framework, while the learning rates for the remaining parameters follow those used in 3D Gaussian Splatting. In addition to the Gaussian Splatting parameters, we also finetune the expression, translation and joint

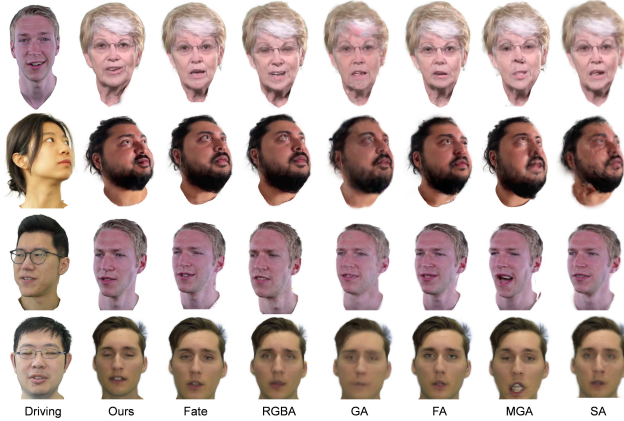


Figure 6. Qualitative results of cross-identity reenactment. Our method accurately animates the source avatar performing expressions such as smiling and eye-closing.

Table 2. Ablation quantitative results on the INSTA dataset.

Method	PSNR $\uparrow$	SSIM $\uparrow$	LPIPS $\downarrow$
w/o Soft Binding	29.66	0.9525	0.0398
w/o ADC	30.31	0.9529	0.0505
w/o FPE-AP	30.38	0.9574	0.0321
w/o FTC	30.43	0.9579	0.0310
w/o Local Decoder $\phi_l$	30.36	0.9575	0.0306
w/o $\mathcal{L}_{vgg}$	30.58	0.9592	0.0426
Ours	30.63	0.9587	0.0304

rotation parameters of FLAME for each timestep as done in GaussianAvatars. As each Gaussian is bound to a mesh triangle, we do not observe noticeable floating Gaussians and thus skip opacity resetting in ADC.

## 4. Experiments

### 4.1. Experimental Setup

**Implementation Details.** We conduct both training and inference on a single NVIDIA RTX 3090 GPU. Each identity’s video is trained for 6 epochs. All videos are cropped and resized to a resolution of  $512 \times 512$ . A robust matting method [15] is applied to extract the foreground with the background set to white. For avatar initialization, we adopt VHAP [19] for monocular head tracking.

**Dataset.** We evaluate our method on four datasets, including INSTA [40], PointAvatar [36], Nerface [4], and HDTF [33], comprising a total of 22 identities. For PointAvatar, we follow the original data split strategy in [36], while for the other datasets, the last 450 frames are reserved as the test set.

**Baselines.** We compare our method against six state-of-the-art Gaussian avatar reconstruction approaches: GaussianAvatars (GA) [20], FateAvatar (Fate) [31], RGAvatar

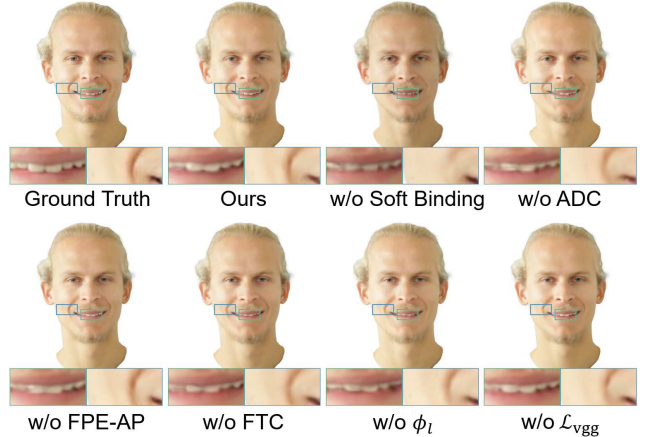


Figure 7. Qualitative results of the ablation study on marcel case. Our full method produces more realistic textures and geometric structures in transiently visible regions, such as the mouth interior, and captures more fine details.

(RGBA) [12], FlashAvatar (FA) [28], MonoGaussianAvatar (MGA) [1], and SplattingAvatar (SA) [24]. Note that simply equalizing or increasing training epochs across methods may not yield optimal results. Accordingly, we follow the settings in the original papers, setting 10 epochs for GA, Fate, and RGBA, 20 for FA, 30 for SA, and 100 for MGA to allow each method to converge properly. Since GA is originally designed for multi-view reconstruction, we adopt various settings from original papers for fair comparison.

### 4.2. Evaluation

**Quantitative Results.** We select PSNR, SSIM, and LPIPS [32] as evaluation metrics to comprehensively assess the visual quality of the reconstructed avatars. As shown in Tab. 1, our method consistently outperforms existing state-of-the-art approaches across most datasets and metrics, achieving notable improvements in reconstruction quality. In particular, our method attains the highest SSIM scores and the lowest LPIPS values on all four datasets, demonstrating its strong ability to preserve both geometric accuracy and perceptual fidelity.

**Qualitative Results.** As shown in Fig. 5, owing to the non-rigid and flexible deformation capability of our UV-Adaptive Soft Binding framework, our method effectively recovers fine-grained details and subtle structures, such as wrinkles and hair. Furthermore, benefiting from the Temporal ADC strategy, our method can produce clearer and higher-quality reconstructions in challenging regions like mouth interiors and eyelids, which are only visible in a subset of frames and are typically difficult to reconstruct. We further evaluate our method on cross-identity reenactment as a real-world test for avatar animation. As illustrated in Fig. 6, our method accurately animates the source avatar performing expressions such as smiling and eye-closing,

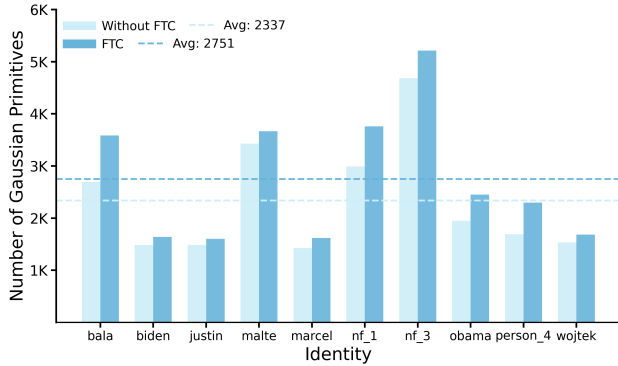


Figure 8. Comparison of Gaussian primitive counts within the mouth interior between the vanilla training strategies and FTC.

while faithfully preserving the identity-specific characteristics and fine-grained details.

### 4.3. Ablation Study

We conduct an ablation study on self-reenactment using the INSTA dataset. The quantitative results are presented in Tab. 2, while the qualitative comparisons are shown in Fig. 7, demonstrating the effectiveness of each component. Additionally, we provide the ablation analysis of all hyper-parameters in the supplementary materials.

**Without Soft Binding.** As shown in Tab. 2 and Fig. 7, removing the Soft Binding framework results in a noticeable degradation across all metrics and visibly poorer reconstruction quality. Relying solely on LBS-based deformation substantially weakens the modeling capability, thereby failing to capture fine-grained details and resulting in blurred teeth as well as the absence of smile-induced facial wrinkles.

**Without ADC.** Removing ADC leads to a significant increase in the LPIPS score, suggesting a degradation in perceptual quality due to the loss of high-frequency details. As shown in Fig. 7, the teeth region and facial wrinkles are insufficiently reconstructed by Gaussians, resulting in overly smooth and less detailed renderings.

**Without FPE-AP.** Replacing FPE-AP criterion with vanilla positional gradient leads to blurred teeth renderings, as the latter considers only geometric information and fails to add Gaussians in regions with high-frequency details.

**Without FTC.** For the vanilla training strategy, we set the densification interval based on the number of clusters to ensure that the total number of densification steps matches that of FTC. The teeth region exhibits incomplete reconstruction due to its transiently visible nature.

**Without Local Decoder  $\phi_l$ .** In this setting, only the global branch is used to model the Gaussian deformation field. As illustrated in Fig. 7, facial wrinkles are reconstructed less accurately, and the teeth region appears blurrier.

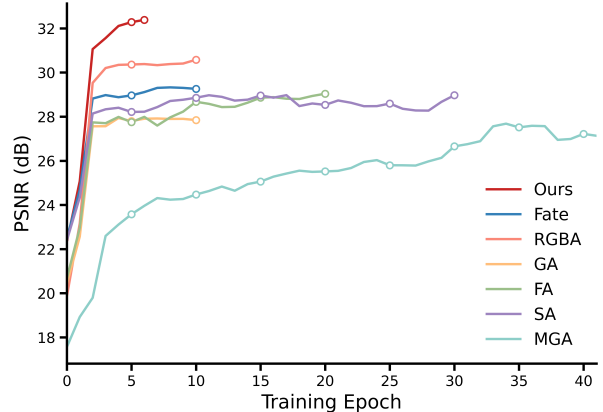


Figure 9. Comparison of PSNR performance across different methods during training. STAvatar exhibits the highest training efficiency among all compared approaches.

**Without  $\mathcal{L}_{vgg}$ .** As shown in Tab. 2, removing the perceptual loss  $\mathcal{L}_{vgg}$  improves SSIM marginally but significantly increases LPIPS score, reflecting overly smooth textures.

### 4.4. Gaussian Number Comparison

To further validate the effectiveness of FTC in transiently visible or frequently occluded regions, we count the number of Gaussian primitives whose UV coordinates fall within the mouth region mask. As illustrated in Fig. 8, we compare the number of Gaussian primitives in the mouth interior with and without FTC on the INSTA dataset. Although some variations exist across identities due to differences in motion and expression within video frames, it is evident that all identities exhibit increased density in the mouth region when using FTC, with an average gain of over 400 primitives (approximately 17%).

### 4.5. Training Efficiency Analysis

As shown in Fig. 9, we present the training progress and corresponding performance measured in terms of PSNR for different methods. The training epochs follow the settings described in Sec. 4.1 to ensure that all methods fully converge. For MonoGaussianAvatar, only the first 40 epochs are reported because its PSNR shows negligible improvement in the later stages of training. In addition, since different methods adopt distinct initialization strategies, their performance at epoch 0 varies accordingly. Notably, our method, STAvatar, exhibits the highest training efficiency among all compared approaches and almost reaches convergence within 6 epochs, surpassing the second-best method by over 2 dB.

## 5. Conclusion

In this paper, we present STAvatar, a novel method for high-fidelity and training-efficient reconstruction of animated

avatars from monocular videos. The proposed UV-Adaptive Soft Binding framework enables flexible and non-rigid deformation field modeling while remaining compatible with the Adaptive Density Control (ADC), thereby effectively capturing subtle expressions and fine-grained details. Besides, our Temporal ADC strategy addresses the limitations of vanilla ADC in dynamic avatar reconstruction, resulting in more accurate and complete reconstructions in frequently occluded regions. Extensive experiments demonstrate that our method significantly outperforms previous approaches in both reconstruction quality and training efficiency.

## References

- [1] Yufan Chen, Lizhen Wang, Qijing Li, Hongjiang Xiao, Shengping Zhang, Hongxun Yao, and Yebin Liu. Monogaussianavatar: Monocular gaussian point-based head avatar. In *ACM SIGGRAPH 2024 Conference Papers*, 2024. [2](#), [3](#), [6](#), [7](#)
- [2] Xiaobin Deng, Changyu Diao, Min Li, Ruohan Yu, and Dunqing Xu. Efficient density control for 3d gaussian splatting. *arXiv preprint arXiv:2411.10133*, 2024. [3](#)
- [3] Bernhard Egger, William AP Smith, Ayush Tewari, Stefanie Wuhler, Michael Zollhoefer, Thabo Beeler, Florian Bernard, Timo Bolkart, Adam Kortylewski, Sami Romdhani, et al. 3d morphable face models—past, present, and future. *ACM Transactions on Graphics (ToG)*, 39(5):1–38, 2020. [1](#)
- [4] Guy Gafni, Justus Thies, Michael Zollhofer, and Matthias Nießner. Dynamic neural radiance fields for monocular 4d facial avatar reconstruction. In *Proceedings of the IEEE/CVF Conference on Computer Vision and Pattern Recognition*, pages 8649–8658, 2021. [7](#)
- [5] Simon Giebenhain, Tobias Kirschstein, Martin Rünz, Lourdes Agapito, and Matthias Nießner. Npga: Neural parametric gaussian avatars. In *SIGGRAPH Asia 2024 Conference Papers*, pages 1–11, 2024. [2](#)
- [6] Philip-William Grassal, Malte Prinzler, Titus Leistner, Carsten Rother, Matthias Nießner, and Justus Thies. Neural head avatars from monocular rgb videos. In *Proceedings of the IEEE/CVF conference on computer vision and pattern recognition*, pages 18653–18664, 2022. [1](#)
- [7] Kaiwen Guo, Peter Lincoln, Philip Davidson, Jay Busch, Xueming Yu, Matt Whalen, Geoff Harvey, Sergio Orts-Escolano, Rohit Pandey, Jason Dourgarian, et al. The relightables: Volumetric performance capture of humans with realistic relighting. *ACM Transactions on Graphics (ToG)*, 38(6):1–19, 2019. [1](#)
- [8] Bernhard Kerbl, Georgios Kopanas, Thomas Leimkühler, and George Drettakis. 3d gaussian splatting for real-time radiance field rendering. *ACM Transactions on Graphics*, 42(4), 2023. [1](#), [2](#), [5](#)
- [9] Shakiba Kheradmand, Daniel Rebain, Gopal Sharma, Weiwei Sun, Yang-Che Tseng, Hossam Isack, Abhishek Kar, Andrea Tagliasacchi, and Kwang Moo Yi. 3d gaussian splatting as markov chain monte carlo. *Advances in Neural Information Processing Systems*, 37:80965–80986, 2024. [3](#)
- [10] Sieun Kim, Kyungjin Lee, and Youngki Lee. Color-cued efficient densification method for 3d gaussian splatting. In *Proceedings of the IEEE/CVF Conference on Computer Vision and Pattern Recognition*, pages 775–783, 2024. [3](#)
- [11] Diederik P Kingma and Jimmy Ba. Adam: A method for stochastic optimization. *arXiv preprint arXiv:1412.6980*, 2014. [6](#)
- [12] Linzhou Li, Yumeng Li, Yanlin Weng, Youyi Zheng, and Kun Zhou. Rgbavatar: Reduced gaussian blendshapes for online modeling of head avatars. In *Proceedings of the Computer Vision and Pattern Recognition Conference*, pages 10747–10757, 2025. [3](#), [6](#), [7](#)
- [13] Tianye Li, Timo Bolkart, Michael J Black, Hao Li, and Javier Romero. Learning a model of facial shape and expression from 4d scans. *ACM Trans. Graph.*, 36(6):194–1, 2017. [3](#)
- [14] Zhanfeng Liao, Yuelang Xu, Zhe Li, Qijing Li, Boyao Zhou, Ruifeng Bai, Di Xu, Hongwen Zhang, and Yebin Liu. Hhavatar: Gaussian head avatar with dynamic hairs. *arXiv e-prints*, pages arXiv–2312, 2023. [3](#)
- [15] Shanchuan Lin, Linjie Yang, Imran Saleemi, and Soumyadip Sengupta. Robust high-resolution video matting with temporal guidance. In *Proceedings of the IEEE/CVF Winter Conference on Applications of Computer Vision*, pages 238–247, 2022. [7](#)
- [16] Di Liu, Teng Deng, Giljoo Nam, Yu Rong, Stanislav Pidrhorskyi, Junxuan Li, Jason Saragih, Dimitris N Metaxas, and Chen Cao. Lucas: Layered universal codec avatars. In *Proceedings of the Computer Vision and Pattern Recognition Conference*, pages 21127–21137, 2025. [3](#)
- [17] Shengjie Ma, Yanlin Weng, Tianjia Shao, and Kun Zhou. 3d gaussian blendshapes for head avatar animation. In *ACM SIGGRAPH 2024 Conference Papers*, pages 1–10, 2024. [3](#)
- [18] Saswat Subhajyoti Mallick, Rahul Goel, Bernhard Kerbl, Markus Steinberger, Francisco Vicente Carrasco, and Fernando De La Torre. Taming 3dgs: High-quality radiance fields with limited resources. In *SIGGRAPH Asia 2024 Conference Papers*, pages 1–11, 2024. [3](#)
- [19] Shenhan Qian. Vhap: Versatile head alignment with adaptive appearance priors, 2024. [1](#), [7](#)
- [20] Shenhan Qian, Tobias Kirschstein, Liam Schoneveld, Davide Davoli, Simon Giebenhain, and Matthias Nießner. Gaussianavatars: Photorealistic head avatars with rigged 3d gaussians. *CVPR*, 2024. [2](#), [3](#), [6](#), [7](#)
- [21] Samuel Rota Bulò, Lorenzo Porzi, and Peter Kotschieder. Revising densification in gaussian splatting. In *European Conference on Computer Vision*, pages 347–362. Springer, 2024. [2](#), [3](#)
- [22] Shunsuke Saito, Gabriel Schwartz, Tomas Simon, Junxuan Li, and Giljoo Nam. Relightable gaussian codec avatars. In *Proceedings of the IEEE/CVF conference on computer vision and pattern recognition*, pages 130–141, 2024. [1](#)
- [23] Jack Saunders, Charlie Hewitt, Yanan Jian, Marek Kowalski, Tadas Baltrusaitis, Yiye Chen, Darren Cosker, Virginia Estellers, Nicholas Gydé, Vinay P Nambodiri, et al. Gasp: Gaussian avatars with synthetic priors. In *Proceedings of the Computer Vision and Pattern Recognition Conference*, pages 271–280, 2025. [3](#)
- [24] Zhijing Shao, Zhaolong Wang, Zhuang Li, Duotun Wang, Xiangru Lin, Yu Zhang, Mingming Fan, and Zeyu Wang.

- SplattingAvatar: Realistic Real-Time Human Avatars with Mesh-Embedded Gaussian Splatting. In *CVPR*, 2024. 2, 6, 7
- [25] Jiapeng Tang, Davide Davoli, Tobias Kirschstein, Liam Schoneveld, and Matthias Niessner. Gaf: Gaussian avatar reconstruction from monocular videos via multi-view diffusion. In *Proceedings of the Computer Vision and Pattern Recognition Conference*, pages 5546–5558, 2025. 1, 3
- [26] Peihao Wang, Yuehao Wang, Dilin Wang, Sreyas Mohan, Zhiwen Fan, Lemeng Wu, Ruisi Cai, Yu-Ying Yeh, Zhangyang Wang, Qiang Liu, et al. Steepest descent density control for compact 3d gaussian splatting. In *Proceedings of the Computer Vision and Pattern Recognition Conference*, pages 26663–26672, 2025. 3
- [27] Zidu Wang, Xiangyu Zhu, Tianshuo Zhang, Baiqin Wang, and Zhen Lei. 3d face reconstruction with the geometric guidance of facial part segmentation. In *Proceedings of the IEEE/CVF Conference on Computer Vision and Pattern Recognition*, pages 1672–1682, 2024. 1
- [28] Jun Xiang, Xuan Gao, Yudong Guo, and Juyong Zhang. Flashavatar: High-fidelity head avatar with efficient gaussian embedding. In *CVPR*, 2024. 2, 3, 6, 7
- [29] Yuelang Xu, Benwang Chen, Zhe Li, Hongwen Zhang, Lizhen Wang, Zerong Zheng, and Yebin Liu. Gaussian head avatar: Ultra high-fidelity head avatar via dynamic gaussians. In *Proceedings of the IEEE/CVF conference on computer vision and pattern recognition*, pages 1931–1941, 2024. 3
- [30] Haotian Yang, Mingwu Zheng, Wanquan Feng, Haibin Huang, Yu-Kun Lai, Pengfei Wan, Zhongyuan Wang, and Chongyang Ma. Towards practical capture of high-fidelity relightable avatars. In *SIGGRAPH Asia 2023 Conference Papers*, pages 1–11, 2023. 1
- [31] Jiawei Zhang, Zijian Wu, Zhiyang Liang, Yicheng Gong, Dongfang Hu, Yao Yao, Xun Cao, and Hao Zhu. Fate: Full-head gaussian avatar with textural editing from monocular video. In *Proceedings of the IEEE/CVF Conference on Computer Vision and Pattern Recognition*, 2025. 2, 3, 6, 7
- [32] Richard Zhang, Phillip Isola, Alexei A Efros, Eli Shechtman, and Oliver Wang. The unreasonable effectiveness of deep features as a perceptual metric. In *Proceedings of the IEEE conference on computer vision and pattern recognition*, pages 586–595, 2018. 7
- [33] Zhimeng Zhang, Lincheng Li, Yu Ding, and Changjie Fan. Flow-guided one-shot talking face generation with a high-resolution audio-visual dataset. In *Proceedings of the IEEE/CVF conference on computer vision and pattern recognition*, pages 3661–3670, 2021. 7
- [34] Zheng Zhang, Wenbo Hu, Yixing Lao, Tong He, and Hengshuang Zhao. Pixel-gs: Density control with pixel-aware gradient for 3d gaussian splatting. In *European Conference on Computer Vision*, pages 326–342. Springer, 2024. 3
- [35] Yufeng Zheng, Victoria Fernández Abrevaya, Marcel C Bühler, Xu Chen, Michael J Black, and Otmar Hilliges. Im avatar: Implicit morphable head avatars from videos. In *Proceedings of the IEEE/CVF conference on computer vision and pattern recognition*, pages 13545–13555, 2022. 1
- [36] Yufeng Zheng, Wang Yifan, Gordon Wetzstein, Michael J. Black, and Otmar Hilliges. Pointavatar: Deformable point-based head avatars from videos. In *Proceedings of the IEEE/CVF Conference on Computer Vision and Pattern Recognition (CVPR)*, 2023. 7
- [37] Hongbi Zhou and Zhangkai Ni. Perceptual-gs: Scene-adaptive perceptual densification for gaussian splatting. *arXiv preprint arXiv:2506.12400*, 2025. 3
- [38] Zheng Zhou, Yu-Jie Xiong, Chun-Ming Xia, Jia-Chen Zhang, and Hong-Jian Zhan. Gradient-direction-aware density control for 3d gaussian splatting. *arXiv preprint arXiv:2508.09239*, 2025. 3
- [39] Wojciech Zielonka, Timo Bolkart, and Justus Thies. Towards metrical reconstruction of human faces. In *European conference on computer vision*, pages 250–269. Springer, 2022. 1
- [40] Wojciech Zielonka, Timo Bolkart, and Justus Thies. Instant volumetric head avatars. In *Conference on Computer Vision and Pattern Recognition*, 2023. 7
- [41] Wojciech Zielonka, Timo Bolkart, Thabo Beeler, and Justus Thies. Gaussian eigen models for human heads. In *Proceedings of the Computer Vision and Pattern Recognition Conference*, pages 15930–15940, 2025. 3

# STAvatar: Soft Binding and Temporal Density Control for Monocular 3D Head Avatars Reconstruction

## Supplementary Material

### 1. Overview

This supplementary material presents additional methodological details, experimental results, and an ethical discussion. Sec. 2 elaborates on offset activation, UV sampling, silhouette coefficient, and the Summed-Area Table. Sec. 3 first provides extended details on the experimental setup for the baseline methods, then visualizes the FTC results to facilitate a more comprehensive understanding, and includes additional ablation studies such as hyperparameter analyses. It also presents further qualitative results and per identity quantitative evaluations. Finally, Sec. 4 discusses data handling practices, potential societal harms, and measures to prevent misuse.

### 2. Method

#### 2.1. Offset Activation Details.

To ensure numerical stability and constrain the influence of the predicted offsets  $\delta_i = \{\delta_\mu, \delta_s, \delta_r, \delta_\alpha, \delta_c\}$  on the final Gaussian parameters, we apply carefully chosen nonlinear activation functions to each component extracted from the UV feature offset map  $\Delta_{map}$ . These activations are designed to restrict each predicted quantity within a semantically meaningful and physically valid range, as described below:

- **Position offset**  $\delta_\mu$ : Given the typical spatial extent of Gaussians, we constrain each component of the position offset to the interval  $[-0.1, 0.1]$  using a hyperbolic tanh activation:

$$\delta_\mu = 0.1 \cdot \tanh(x), \quad (1)$$

where  $x \in \mathbb{R}^3$  is the raw network output.

- **Scaling Offset**  $\delta_s$ : To ensure the scaling offset remains strictly positive—thus making the multiplication with the coarse scale  $\tilde{s}$  valid—we apply an exponential activation to map the output to the range  $(0, +\infty)$ :

$$\delta_s = \exp(x), \quad (2)$$

where  $x \in \mathbb{R}^3$ . The final scale is computed as the element-wise product of  $\delta_s$  and the coarsely deformed scale  $\tilde{s}$ , ensuring both positivity and flexible control.

- **Rotation offset**  $\delta_r$ : The raw rotation offset is represented as an axis-angle vector  $x \in \mathbb{R}^3$ . Its magnitude is first normalized to the interval  $[-\pi, \pi]$  via:

$$\delta_r^{\text{angle}} = \pi \cdot \tanh(x), \quad (3)$$

and then converted to a unit quaternion  $\delta_r$  using the standard axis-angle to quaternion transformation. This guarantees a valid rotation that can be composed with the coarsely deformed rotation  $\tilde{r}$  through the Hamilton product.

- **Opacity offset**  $\delta_\alpha$ : To avoid drastic changes in transparency, the opacity offset is constrained to  $[-0.5, 0.5]$ :

$$\delta_\alpha = 0.5 \cdot \tanh(x), \quad (4)$$

where  $x \in \mathbb{R}$ . After adding  $\delta_\alpha$  to the coarse opacity  $\tilde{\alpha}$ , the final opacity  $\alpha^*$  is further clamped to  $[0, 1]$  to ensure physical plausibility.

- **Color offset**  $\delta_c$ : To limit abrupt color shifts during Gaussian’s deformation, we restrict each channel of the color offset to  $[-0.7, 0.7]$  via:

$$\delta_c = 0.7 \cdot \tanh(x), \quad (5)$$

with  $x \in \mathbb{R}^3$ .

These bounded activations not only prevent degenerate parameter updates during training (e.g., negative scale or invalid quaternion norms), but also provide a consistent prior for Gaussian parameters, allowing more effective learning from the UV-space offset map  $\Delta_{map}$ .

#### 2.2. UV Sample.

As shown in Algorithm 1, we provide a more detailed algorithmic description of UV-Adaptive Sampling. Since certain mesh triangles may not cover any valid pixels after UV rasterization, it becomes infeasible to define the UV coordinates of the associated Gaussian primitives using pixel-based sampling. To address this, we incorporate an analytical fallback strategy that samples barycentric coordinates uniformly within the triangle, enabling the assignment of UV coordinates even when no valid pixels are present.

As illustrated in Fig. 1, after applying Temporal Adaptive Density Control, our UV-Adaptive Sampling adaptively allocates more Gaussians to regions requiring finer details across different identities. In particular, the central facial region of *biden* contains more points due to the presence of facial wrinkles, which demand higher density. Additionally, the density in *nf\_01*’s eye region significantly increases because *nf\_01* wears glasses, which typically require more Gaussians for accurate modeling.

#### 2.3. Silhouette Coefficient.

To determine an appropriate number of clusters  $K$  for grouping structurally similar frames based on FLAME [4]

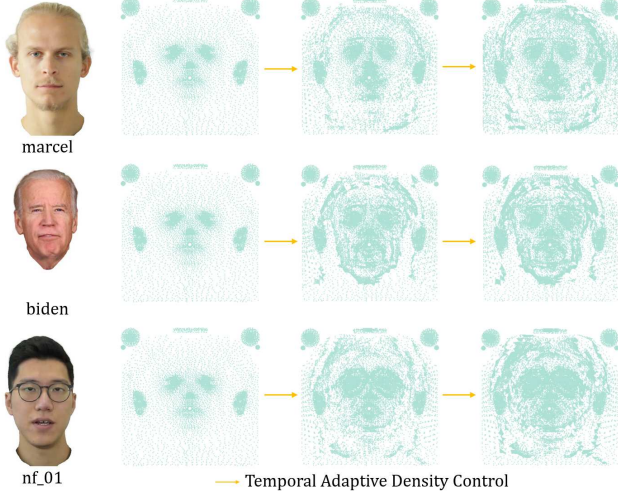


Figure 1. Visualization of UV-Adaptive Sampling’s points.

parameters, we adopt the Silhouette Coefficient as the selection metric. Given a data point  $i$ , the silhouette score  $s(i)$  is defined as:

$$s(i) = \frac{b(i) - a(i)}{\max\{a(i), b(i)\}}, \quad s(i) \in [-1, 1], \quad (6)$$

where  $a(i)$  denotes the mean intra-cluster distance of point  $i$ , and  $b(i)$  represents the smallest mean distance between point  $i$  and all points in the nearest neighboring cluster. These quantities are computed as:

$$a(i) = \frac{1}{|C_i| - 1} \sum_{\substack{j \in C_i \\ j \neq i}} d(i, j), \quad (7)$$

$$b(i) = \min_{k \neq i} \left( \frac{1}{|C_k|} \sum_{j \in C_k} d(i, j) \right), \quad (8)$$

where  $C_i$  is the cluster to which point  $i$  belongs, and  $d(i, j)$  denotes the Euclidean distance in the PCA-projected FLAME parameter space. A higher average silhouette score across all points indicates better-defined and more compact clustering. We evaluate the silhouette score across varying  $K \in [5, 12]$ , and select the value that maximizes the overall score.

## 2.4. Summed-Area Table.

To efficiently compute aggregated error values over rectangular regions in the screen-space image domain, we adopt the two-dimensional *Summed-Area Table (SAT)* strategy, also known as the *integral image*. This data structure allows the summation of any axis-aligned rectangular region in constant time using only four memory accesses.

Given an input error map  $E \in \mathbb{R}^{H \times W}$ , where  $H$  and  $W$  denote the image height and width, respectively, the SAT

---

### Algorithm 1 UV-Adaptive Sampling

---

**Input:**

$\mathcal{B} \in \mathbb{N}^N$ : face binding index per Gaussian  
 $\mathcal{V}_{uv} \in \mathbb{R}^{V \times 2}$ : UV coordinates of mesh vertices  
 $\mathcal{F}_{uv} \in \mathbb{N}^{F \times 3}$ : triangle face indices over UV mesh  
 $R$ : UV rasterization resolution (e.g.,  $R = 256$ )

**Output:**

$\mathcal{U} \in \mathbb{R}^{N \times 2}$ : UV coordinates per Gaussian

- 1: Rasterize UV mesh  $(\mathcal{V}_{uv}, \mathcal{F}_{uv})$  into  $R \times R$  grid  
 $\rightarrow (\mathcal{M}_{face}, \mathcal{M}_{bary}) \in \mathbb{Z}^{R \times R}, \mathbb{R}^{R \times R \times 3}$
  - 2: Initialize per-face pixel pool map  $\mathcal{P}[f] \leftarrow \emptyset, \forall f \in \mathcal{F}_{uv}$
  - 3: **for** each pixel  $(i, j)$  where  $\mathcal{M}_{face}[i, j] \neq -1$  **do**
  - 4:  $f \leftarrow \mathcal{M}_{face}[i, j]$
  - 5: Append  $(i, j), \mathcal{M}_{bary}[i, j]$  into  $\mathcal{P}[f]$
  - 6: **end for**
  - 7: Faces with valid pixels:  $\mathcal{F}_{valid} \leftarrow \{f \mid \mathcal{P}[f] \neq \emptyset\}$
  - 8: Initialize barycentric buffer  $\mathbf{b} \in \mathbb{R}^{N \times 3}$ , face index buffer  $\mathbf{f}_{idx} \in \mathbb{N}^N$
  - 9: **for** each face  $f$  that appears in bindings  $\mathcal{B}$  **do**
  - 10:  $\mathcal{I}_f \leftarrow \{i \mid \mathcal{B}[i] = f\}$  {Indices of points bound to  $f$ }
  - 11:  $C_f \leftarrow \lfloor \mathcal{I}_f \rfloor$
  - 12: **if**  $f \in \mathcal{F}_{valid}$  **then**
  - 13: *Pixel-based Sampling*
  - 14: Let  $\mathbf{p}_f$  be sorted pixel list of face  $f$  in  $\mathcal{P}[f]$
  - 15: **if**  $|\mathbf{p}_f| \geq C_f$  **then**
  - 16: Select  $C_f$  evenly spaced pixels from  $\mathbf{p}_f$
  - 17: **else**
  - 18: Select all  $|\mathbf{p}_f|$  pixels and sample extra with replacement to reach  $C_f$
  - 19: **end if**
  - 20: Extract barycentric coordinates  $\mathbf{b}_f$  from  $\mathcal{P}[f]$
  - 21: **else**
  - 22: *Analytical Sampling*
  - 23: **for**  $i = 1$  to  $C_f$  **do**
  - 24: Sample  $u, v \sim \mathcal{U}(0, 1)$
  - 25: Compute:  $b_0 = 1 - \sqrt{u}$ ,  $b_1 = \sqrt{u}(1 - v)$ ,  $b_2 = \sqrt{uv}$
  - 26: Append  $[b_0, b_1, b_2]$  to  $\mathbf{b}_f$
  - 27: **end for**
  - 28: **end if**
  - 29: Assign:  $\mathbf{b}[\mathcal{I}_f] \leftarrow \mathbf{b}_f$ ,  $\mathbf{f}_{idx}[\mathcal{I}_f] \leftarrow f$
  - 30: **end for**
  - 31:  $\mathcal{U} \leftarrow \text{BarycentricReweight}(\mathcal{V}_{uv}, \mathcal{F}_{uv}, \mathbf{f}_{idx}, \mathbf{b})$
- 

$I \in \mathbb{R}^{(H+1) \times (W+1)}$  is constructed as:

$$I(u, v) = \sum_{y=0}^{u-1} \sum_{x=0}^{v-1} E(y, x), \quad (9)$$

with the boundary conditions  $I(0, v) = I(u, 0) = 0$  for

all  $u, v$ , which provide zero-padding to simplify index handling. The SAT is built in a single pass using two cumulative summations:

1. Compute the row-wise prefix sum for each row.
2. Compute the column-wise prefix sum of the row-wise sums.

This process is equivalent to:

$$I(u+1, v+1) = E(u, v) + I(u, v+1) + I(u+1, v) - I(u, v) \quad (10)$$

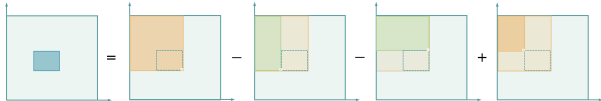


Figure 2. Inclusion–exclusion principle

Once the SAT is constructed, the sum over any rectangular region  $[x_1, x_2] \times [y_1, y_2]$  can be computed in constant time using:

$$\sum_{x=x_1}^{x_2} \sum_{y=y_1}^{y_2} E(y, x) = I(y_2+1, x_2+1) - I(y_1, x_2+1) - I(y_2+1, x_1) + I(y_1, x_1). \quad (11)$$

This formula leverages the inclusion–exclusion principle to compute the sum via four corner indices, as illustrated in Fig. 2. The SAT reduces the computational complexity from  $\mathcal{O}(R^2)$  per Gaussian to  $\mathcal{O}(1)$  per region, enabling efficient error accumulation for tens or hundreds of thousands of Gaussians in real-time optimization.

### 3. Experiments

#### 3.1. Baselines

As stated in the main paper, the number of training epochs is set to 10 for GA [5], RGBA [3] and Fate [9], 20 for FA [8], 30 for SA [6] and 100 for MGA [1] to ensure convergence. Except for the PointAvatar [11] dataset, we follow Fate’s training schedule by training all baseline methods for 50 epochs and our method, STAvatar, for 30 epochs. Additionally, following the DECA-based [2] preprocessing pipeline, we further refine the FLAME coefficients for 50 epochs using a learning rate of  $5 \times 10^{-4}$  during testing, which is consistent with the IMAvatar [10] protocol.

#### 3.2. t-SNE of FTC.

To intuitively demonstrate the effectiveness of our FTC strategy, we visualize the clustering results using t-SNE [7] in Fig. 3. The number of clusters  $K$  is adaptively determined using the silhouette coefficient, which allows FTC to dynamically adjust to the inherent data distribution across identities. As shown in the Fig. 3, embeddings belonging to

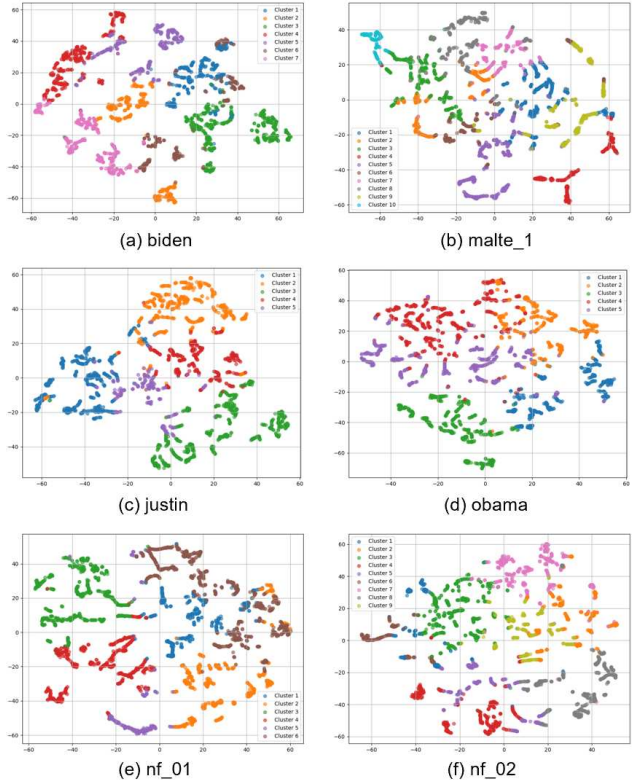


Figure 3. t-SNE visualization of different identities after applying FTC. Each color represents a distinct video frame cluster.

different identities are clearly separated in the latent space, suggesting that FTC effectively groups structurally similar frames into coherent clusters, which facilitates the computation of the average densification criterion.

Table 1. Hyperparameter ablation results. The row in **bold** indicates the configuration used in the main paper: FPE’s  $\mathcal{L}_{d-ssim}$  weight  $\lambda_1 = 0.2$ , FTC’s randomly training epochs  $M = 1$ , and FTC’s cluster weights (0.3, 0.6, 0.1).

Hyperparameter	Setting	Metrics		
		PSNR $\uparrow$	SSIM $\uparrow$	LPIPS $\downarrow$
$\lambda_1$	0.1	30.52	0.9577	0.0312
	0.3	30.48	0.9579	0.0311
	<b>0.2</b>	30.63	0.9587	0.0304
$M$	2	30.53	0.9582	0.0310
	0	30.42	0.9572	0.0311
	<b>1</b>	30.63	0.9587	0.0304
cluster weights	(0.5, 0.4, 0.1)	30.44	0.9584	0.0312
	(0.4, 0.5, 0.1)	30.50	0.9583	0.0311
	<b>(0.3, 0.6, 0.1)</b>	30.63	0.9587	0.0304

### 3.3. Additional Ablation Study

We conduct additional ablation studies to further validate the effectiveness of each proposed component and the selection of key hyper-parameters. All results are summarized in Tab. 1, where we compare multiple candidate settings for the FPE’s  $\mathcal{L}_{d\text{-ssim}}$  weight, the FTC’s randomly training epochs  $M$ , and the FTC’s cluster weights. The configuration adopted in the main paper is indicated in bold.

**FPE:  $\mathcal{L}_{d\text{-ssim}}$  weight.** We examine three choices for the perceptual weighting coefficient. The setting  $\lambda_1 = 0.2$  consistently achieves the highest PSNR, SSIM, and lowest LPIPS, demonstrating that it provides a more balanced trade-off between pixel-level reconstruction and perceptual fidelity. This result aligns with the intuition that moderate perceptual emphasis yields better alignment with human visual sensitivity.

**FTC: Randomly training epochs  $M$ .** We further evaluate the influence of the FTC training strategy by varying the number of random training epochs  $M$ . The configuration  $M = 1$  produces the best performance, indicating that performing clustered training followed by a single fine-tuning epoch on the entire training set is sufficient and effective. This observation verifies the necessity and contribution of FTC in facilitating the computation of the densification criterion which benefits the reconstruction of transiently visible regions.

**FTC: Cluster weights.** Besides, we test different FLAME-based cluster weight combinations to assess their impact on the clustering quality. The best-performing setting (0.3, 0.6, 0.1) (corresponding to expression, pose, and translation components) assigns a larger weight to pose-related components, highlighting that pose cues dominate the temporal variations relevant to our densification criterion. This confirms that emphasizing pose information improves the reliability of cluster formation and benefits the downstream optimization process.

### 3.4. Self-Reenactment

As shown in Fig. 4, STAvatar reconstructs fine-grained geometric and appearance details (e.g., hair strands, eye contours, and glasses frames) more faithfully than prior approaches. With the assistance of Temporal Adaptive Density Control, our model allocates higher density to transient or frequently occluded regions, leading to improved reconstruction of structures such as teeth. As summarized in Tab. 2 and Tab. 3, although STAvatar does not outperform all baselines on every metric, it achieves the best overall performance on all datasets.

### 3.5. Cross-Reenactment

As illustrated in Fig. 5, our method accurately transfers diverse expressions and motions—such as eye-closing, mouth asymmetry, and pouting—from the source actor while pre-

serving the target identity’s geometry and appearance. Even under significant pose variations and complex non-rigid deformations, the reconstructed avatars retain stable identity-related geometry and appearance, demonstrating the robustness of the proposed soft binding and temporal density control.

## 4. Ethical Discussion

All datasets used in this study are publicly available and collected in compliance with their respective licenses. While our method enables the generation of realistic and controllable 3D head avatars, we acknowledge its potential misuse in fabricating synthetic content that may infringe on privacy or mislead the public. We explicitly oppose any use of this technology for malicious or unauthorized purposes, including identity fraud or deceptive media creation. Developers and practitioners should act responsibly and follow ethical guidelines to prevent potential harm from misuse.

## References

- [1] Yufan Chen, Lizhen Wang, Qijing Li, Hongjiang Xiao, Shengping Zhang, Hongxun Yao, and Yebin Liu. Monogaussianavatar: Monocular gaussian point-based head avatar. In *ACM SIGGRAPH 2024 Conference Papers*, 2024. 3
- [2] Yao Feng, Haiwen Feng, Michael J Black, and Timo Bolkart. Learning an animatable detailed 3d face model from in-the-wild images. *ACM Transactions on Graphics (ToG)*, 40(4): 1–13, 2021. 3
- [3] Linzhou Li, Yumeng Li, Yanlin Weng, Youyi Zheng, and Kun Zhou. Rgbavatar: Reduced gaussian blendshapes for online modeling of head avatars. In *Proceedings of the Computer Vision and Pattern Recognition Conference*, pages 10747–10757, 2025. 3
- [4] Tianye Li, Timo Bolkart, Michael J Black, Hao Li, and Javier Romero. Learning a model of facial shape and expression from 4d scans. *ACM Trans. Graph.*, 36(6):194–1, 2017. 1
- [5] Shenhan Qian, Tobias Kirschstein, Liam Schoneveld, Davide Davoli, Simon Giebenhain, and Matthias Nießner. Gaussianavatars: Photorealistic head avatars with rigged 3d gaussians. *CVPR*, 2024. 3
- [6] Zhijing Shao, Zhaolong Wang, Zhuang Li, Duotun Wang, Xiangru Lin, Yu Zhang, Mingming Fan, and Zeyu Wang. SplattingAvatar: Realistic Real-Time Human Avatars with Mesh-Embedded Gaussian Splatting. In *CVPR*, 2024. 3
- [7] Laurens van der Maaten, Geoffrey Hinton, and Yoesoep Rachmad. Visualizing data using t-sne. *Journal of Machine Learning Research*, 9:2579–2605, 2008. 3
- [8] Jun Xiang, Xuan Gao, Yudong Guo, and Juyong Zhang. Flashavatar: High-fidelity head avatar with efficient gaussian embedding. In *CVPR*, 2024. 3
- [9] Jiawei Zhang, Zijian Wu, Zhiyang Liang, Yicheng Gong, Dongfang Hu, Yao Yao, Xun Cao, and Hao Zhu. Fate: Full-head gaussian avatar with textural editing from monocular video. In *Proceedings of the IEEE/CVF Conference on Computer Vision and Pattern Recognition*, 2025. 3



Figure 4. Qualitative comparisons of head reconstruction results across different state-of-the-art methods. Our method STAvatar produces more accurate geometry and fine-grained details, particularly in challenging regions such as occluded inner mouth areas.

- [10] Yufeng Zheng, Victoria Fernández Abrevaya, Marcel C. Bühler, Xu Chen, Michael J. Black, and Otmar Hilliges. I M Avatar: Implicit morphable head avatars from videos. In *Computer Vision and Pattern Recognition (CVPR)*, 2022. 3
- [11] Yufeng Zheng, Wang Yifan, Gordon Wetzstein, Michael J. Black, and Otmar Hilliges. Pointavatar: Deformable point-

based head avatars from videos. In *Proceedings of the IEEE/CVF Conference on Computer Vision and Pattern Recognition (CVPR)*, 2023. 3

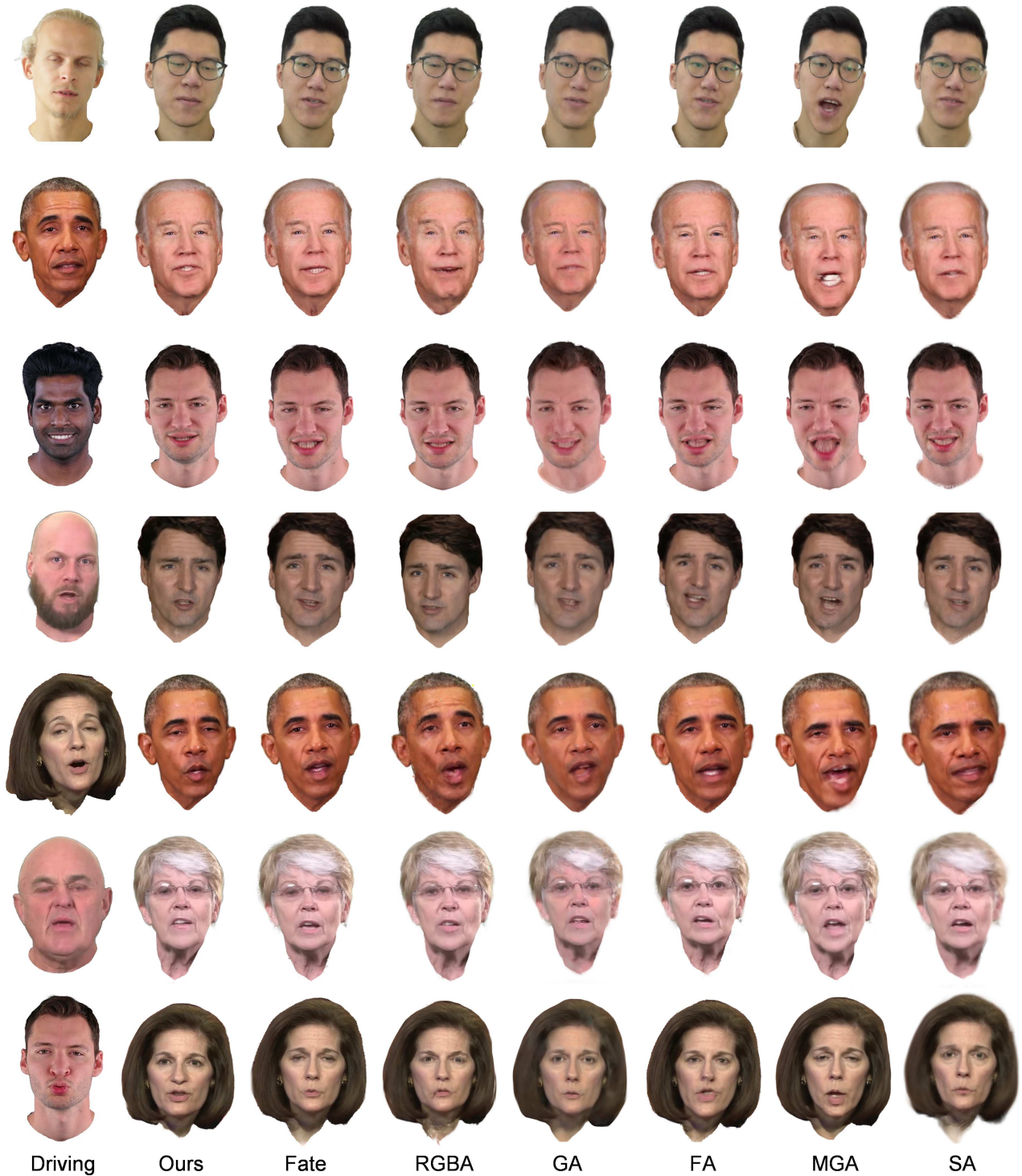


Figure 5. Qualitative comparison of cross-reenactment results with state-of-the-art methods. Our approach achieves faithful expression transfer while maintaining consistent identity-specific geometry and appearance.

Table 2. Full comparison of quantitative results with state-of-the-art methods on INSTA dataset.

Datasets		INSTA Dataset									
		bala	biden	justin	malte_1	marcel	nf.01	nf.03	obama	person_4	wojtek_1
PSNR↑	SplattingAvatar	27.01	29.25	28.01	27.97	29.02	24.59	27.59	23.83	27.19	30.35
	MonoGaussianAvatar	25.39	29.38	27.32	28.25	28.27	25.09	28.01	27.10	24.48	30.16
	GaussianAvatars	27.41	29.11	27.49	27.69	27.84	23.71	27.27	23.40	26.04	29.89
	FlashAvatar	28.86	28.95	27.20	28.46	29.07	24.90	27.87	27.24	25.80	30.61
	RGBAvatar	29.11	30.45	28.48	28.39	30.56	26.44	27.95	27.53	24.53	30.65
	FateAvatar	29.02	30.28	28.54	28.35	29.21	25.40	28.20	27.93	25.40	30.94
	Ours	29.26	32.79	29.16	31.73	32.54	28.38	30.72	31.48	29.23	30.98
SSIM↑	SplattingAvatar	0.9138	0.9498	0.9570	0.9326	0.9325	0.9225	0.9133	0.9158	0.9452	0.9466
	MonoGaussianAvatar	0.8956	0.9546	0.9577	0.9386	0.9322	0.9324	0.9205	0.9426	0.9273	0.9498
	GaussianAvatars	0.9287	0.9551	0.9589	0.9356	0.9370	0.9242	0.9179	0.9205	0.9488	0.9516
	FlashAvatar	0.9187	0.9519	0.9513	0.9345	0.9298	0.9307	0.9162	0.9401	0.9377	0.9457
	RGBAvatar	0.9432	0.9685	0.9705	0.9470	0.9452	0.9488	0.9314	0.9542	0.9255	0.9591
	FateAvatar	0.9299	0.9646	0.9641	0.9438	0.9403	0.9384	0.9193	0.9511	0.9398	0.9552
	Ours	0.9406	0.9757	0.9706	0.9584	0.9541	0.9524	0.9481	0.9724	0.9575	0.9571
LPIPS↓	SplattingAvatar	0.1386	0.0771	0.0811	0.0839	0.1042	0.1325	0.1294	0.1126	0.1101	0.0769
	MonoGaussianAvatar	0.1135	0.0486	0.0539	0.0639	0.1338	0.1058	0.1098	0.0581	0.1151	0.0563
	GaussianAvatars	0.0976	0.0593	0.0655	0.0714	0.1032	0.1049	0.1138	0.0854	0.0908	0.0593
	FlashAvatar	0.0405	0.0315	0.0384	0.0401	0.0775	0.0692	0.0642	0.0407	0.1258	0.0347
	RGBAvatar	0.0535	0.0260	0.0327	0.0409	0.0655	0.0577	0.0666	0.0364	0.1029	0.0361
	FateAvatar	0.0534	0.0338	0.0360	0.0412	0.0681	0.0714	0.0603	0.0400	0.0691	0.0351
	Ours	0.0378	0.0166	0.0249	0.0234	0.0432	0.0406	0.0346	0.0182	0.0386	0.0256

Table 3. Full comparison of quantitative results with state-of-the-art methods on the HDFT dataset, PointAvatar dataset, and NerFace dataset.

Datasets		HDFT Dataset					PointAvatar Dataset			NerFace Dataset			
		subject1	subject2	subject3	subject4	subject5	subject6	yufeng	marcel	soubhik	person1	person2	person3
PSNR↑	SplattingAvatar	27.30	31.46	30.04	29.08	19.71	18.52	25.06	26.17	23.55	24.59	26.24	27.59
	MonoGaussianAvatar	28.57	32.89	30.30	30.15	20.42	19.92	28.86	25.90	28.97	25.09	26.46	28.01
	GaussianAvatars	26.21	31.06	29.63	28.69	18.16	16.74	24.93	26.15	22.77	23.71	26.25	27.27
	FlashAvatar	28.88	32.77	29.25	30.13	20.37	19.60	25.86	26.04	26.67	24.90	28.10	27.87
	RGBAvatar	28.83	30.30	29.57	29.44	20.97	21.23	26.34	27.35	26.32	26.44	26.99	27.95
	FateAvatar	28.98	33.10	30.59	30.24	20.52	19.66	29.07	26.77	29.25	25.40	27.75	28.20
	Ours	30.38	34.39	32.54	28.45	20.76	21.11	27.85	28.81	28.10	28.38	31.14	30.72
SSIM↑	SplattingAvatar	0.8827	0.9679	0.9556	0.9421	0.8366	0.7684	0.8757	0.9198	0.8858	0.9225	0.9357	0.9133
	MonoGaussianAvatar	0.9164	0.9745	0.9588	0.9553	0.8743	0.8231	0.9258	0.9154	0.9419	0.9324	0.9469	0.9205
	GaussianAvatars	0.8826	0.9687	0.9571	0.9447	0.8400	0.7341	0.8904	0.9302	0.9014	0.9242	0.9417	0.9179
	FlashAvatar	0.9198	0.9728	0.9488	0.9538	0.8592	0.8114	0.8870	0.9126	0.9169	0.9307	0.9524	0.9162
	RGBAvatar	0.9347	0.9705	0.9618	0.9598	0.8806	0.8588	0.9020	0.9288	0.9343	0.9488	0.9513	0.9314
	FateAvatar	0.9256	0.9747	0.9593	0.9554	0.8700	0.8271	0.9223	0.9254	0.9385	0.9384	0.9515	0.9193
	Ours	0.9456	0.9826	0.9719	0.9562	0.8799	0.8522	0.9236	0.9348	0.9426	0.9524	0.9697	0.9481
LPIPS↓	SplattingAvatar	0.1753	0.0638	0.1167	0.1200	0.3096	0.3070	0.1512	0.1388	0.1534	0.1325	0.0817	0.1294
	MonoGaussianAvatar	0.1081	0.0471	0.0977	0.0997	0.1776	0.2049	0.0958	0.1552	0.0830	0.1058	0.0545	0.1098
	GaussianAvatars	0.1502	0.0617	0.1115	0.1237	0.2446	0.3661	0.1397	0.1263	0.1340	0.1049	0.0709	0.1138
	FlashAvatar	0.0639	0.0296	0.0794	0.0578	0.1200	0.1139	0.1100	0.1051	0.0690	0.0692	0.0331	0.0642
	RGBAvatar	0.0595	0.0327	0.0617	0.0503	0.1532	0.1351	0.0872	0.0767	0.1011	0.0577	0.0408	0.0666
	FateAvatar	0.0638	0.0320	0.0643	0.0694	0.1389	0.1413	0.0709	0.0960	0.0660	0.0714	0.0356	0.0603
	Ours	0.0356	0.0160	0.0275	0.0410	0.1162	0.0893	0.0505	0.0576	0.0404	0.0406	0.0180	0.0346